Field-dependent AC susceptibility and transport measurements on CuNi near the ferromagnetic percolation threshold

1998 J. Phys.: Condens. Matter 10 6771

(http://iopscience.iop.org/0953-8984/10/30/016)

J. Phys.: Condens. Matter **10** (1998) 6771–6793. Printed in the UK PII: S0953-8984(98)93536-6

Field-dependent AC susceptibility and transport measurements on CuNi near the ferromagnetic percolation threshold

P A Stampe†‡ and Gwyn Williams†

† Department of Physics and Astronomy, University of Manitoba, Winnipeg MB, R3T 2N2, Canada

‡ Department of Physics, Florida A&M University, Tallahassee, FL 32307, USA

Received 22 April 1998

Abstract. A summary of field- and temperature-dependent ac susceptibility and of low-field resistive anisotropy (LFRA) measurements on the CuNi system is presented. Detailed analyses of these data, along with those from zero-field resistivity measurements, yield an estimate for the critical composition above which ferromagnetism appears of $c_0 = 44.5$ at.% Ni; this confirms the value deduced previously from measurements of the spontaneous resistive anisotropy on the same samples. The general features of these data are consistent with a quasi-localized moment description of this system, with a distribution of exchange coupling strengths between such moments. For an (assumed) Gaussian distribution, the trends evident in both the exponent values deduced from susceptibility data and the LFRA are those expected when the ratio η of the first to second moment of this distribution decreases towards unity as c_0 is approached from above.

1. Introduction

The appearance of ferromagnetism in the binary CuNi system with increasing Ni concentration is a subject of long-standing interest, in terms of both the appropriate description of the evolution of this effect and the specific, critical composition above which the transition appears. For many decades CuNi was regarded as a textbook example of a band ferromagnet, its magnetization explained by the rigid band model [1]. More recent work argued against this simple explanation, and it appears currently that many aspects of the magnetic and transport properties of this system are better described in terms of quasi-localized moments [2–5]. Several approaches have linked such moments with local environmental effects, specifically with statistically rich Ni regions [3–6] treated typically with a Jaccarino–Walker style model.

Amongst the magnetically ordered 3d transition elements Ni is unique in *not* displaying a magnetic moment when incorporated as an isolated impurity in a non-magnetic host [7]. The appropriate model framework to describe this result is, again, unresolved, with the variety of theoretical approaches being best illustrated in the case of dilute PdNi. Here isolated Ni atoms have been categorized as non-magnetic as a result of: (i) an inability to satisfy the static Hartree–Fock criterion for magnetism (nevertheless strong local exchange enhancement stabilizes relatively long-lived local spin fluctuations) [8–10]; (ii) interconfigurational fluctuations between nearly degenerate non-magnetic (d^{10}) and magnetic (d^9) many electron Ni configurations at low temperatures [11] or (iii) the

0953-8984/98/306771+23$19.50

Kondo compensation of a single such (energetically stable) magnetic configuration [12]. Irrespective of which model is ultimately judged to be correct, this unique state for isolated Ni atoms does lead to an unusual magnetic phase diagram for such systems in the concentration (c)–temperature plane.

Magnetic order results from interaction effects; in the case of PdNi, the well established critical composition (c_0) for the onset of long-ranged ferromagnetism is [13–15] $c_0 = 2.3 \pm 0.05$ at.% Ni. In this latter system—as in CuNi—local environmental effects are important; however, the description of the ensuing magnetic order by inhomogeneous models (in which near neighbour pairs—or triplets—are magnetic, with interactions predominating between such clusters [16–20]) has been questioned by a comprehensive re-analysis of magnetic data [12]. The latter concludes that this system is a 'magnetically homogeneous' one in that the onset of ferromagnetism is controlled principally by interactions between isolated (but fluctuating) Ni moments. Here the absence of spin-glass order below c_0 constituted the principal argument against the inhomogeneous approach.

In the CuNi system the critical concentration c_0 has been variously estimated at between 43 and 48 at.% Ni [21, 22]. This is some twenty times larger than for Ni in Pd, and raises the question of whether a description of this system in terms of CPA type bands, within which a modified Stoner type criterion for the existence of ferromagnetism is applicable. Again statistical (environmental) fluctuations are thought to play an important role, so that here localized exchange enhancement effects are envisaged as becoming large enough in some more extended region to enable a 'cluster' moment to be stabilized, for which the characteristic energy scale will reflect interactions *within* this more extended region of statistically higher Ni site occupation, rather than the single site-conduction electron coupling strength characterizing the Kondo temperature ($\sim$50 K) of isolated Ni sites in Pd. Within such a picture the possibility has been raised that RKKY type interactions, mediated by the conduction electrons, between stable 'cluster' moments might occur, resulting in a cluster (spin) glass-like ordered regime (the ordering temperature reflecting the strength of this inter moment coupling) immediately below c_0 prior to the establishment of long-range ferromagnetic order [21, 23]. In this latter context, the question arises of whether the inhomogeneity evident in neutron scattering data in this concentration range [3, 24] is simply a manifestation of the importance statistical fluctuations must play immediately above c_0 (where the ferromagnetic ordering temperature T_c approaches zero, and the measuring temperature is comparable with T_c so that the effects of short-range order become increasingly important) or whether indeed it reflects the presence of a more complex magnetic state.

Perhaps the most convincing evidence to date to support the existence of a 'complex' (non-ferromagnetic) state below about 45 at.% Ni has been provided by zero-field ac susceptibility measurements [23]. However in the time that has elapsed since the publication of these data it has been recognized that both the specimen geometry [25] and the application of superimposed static biasing fields [25, 26] can play an important role in such measurements, and hence in identifying the associated moment structure. Here we present the results of two unconventional measurements—the field dependent ac susceptibility and the low-field magnetoresistive anisotropy—on CuNi samples for which the effects of demagnetizing constraints have been deliberately minimized, along with zero-field resistivity measurements. These data, and their analysis, are summarized below.

2. Experimental details

Sixteen specimens with nominal compositions between 45 and 55 at.% Ni were prepared by arc melting using high-purity starting materials. Buttons of the highest and lowest

concentrations were made initially, and samples with intermediate composition prepared subsequently by melting together appropriate amounts of these two end members. To ensure homogeneity each button was inverted and remelted five times, after which they were cold-rolled (between protective Melinex plastic sheets) to a thickness of about 0.2 mm. Samples of approximate dimensions $(16 \times 2 \times 0.2)$ mm^3—suitable for susceptibility measurements—and $(40 \times 2 \times 0.2)$ mm^3—suitable for transport measurements—were cut from these sheets. Following etching (to remove possible surface contamination) and washing, these samples were annealed for 48 h *in vacuo* at 950 °C and water quenched immediately before measuring; such a treatment was chosen to minimize the presence of Ni clusters [27]. It was from such sheets with the lowest and highest compositions that intermediate concentrations were formed.

The ac susceptibility $\chi(H, T)$ was measured in a phase-locked susceptometer [26, 28] operating at 2.4 kHz with driving fields of 5 μT rms applied parallel to the longest dimensions; static biasing fields up to 0.1 T could be superimposed on the ac driving field by a coaxially mounted solenoid; data were collected using a personal computer with a GPIB card. Temperatures below about 10 K were measured using a calibrated Ge thermometer (Cryocal Inc. CR2500H) and those above 10 K by a Au + 0.03 at.% Fe versus chromel P thermocouple; each sensor was in good thermal contact with the specimen [26]. Corrections made for the internal field were based on demagnetization factors (N) estimated by treating each sample as an ellipsoid with principal axes equal to the measured dimensions and evaluating the corresponding elliptic integral [26, 29]; these factors were deliberately chosen to be small, for the reasons discussed below.

The zero-field resistance $\rho(T)$ was measured using a high-precision ac (37 Hz) technique in which fractional changes of 1 in 10^5 (or better) can be resolved [15]; currents of typically 1–10 mA were applied along the largest specimen dimension. Temperatures could be stabilized using a variable feedback loop incorporating a calibrated Ge resistor (Lakeshore Cryogenics 2000), and subsequently measured using the latter and a gas thermometer (with an accuracy estimated at better than 1%). This latter cryostat was also used to measure the low field resistive anisotropy (LFRA), i.e. the difference in resistivity with a field ($\leqslant 10^{-2}$ T) applied first parallel and then perpendicular to the sample current direction. These fields were applied using an externally mounted, rotatable Helmholtz coil arrangement energized by a stabilized current source. The high-field magnetoresistance in both the longitudinal ($\rho_\parallel$) and transverse ($\rho_\perp$) mode had been measured in a separate cryostat, as reported previously [22].

3. Results and discussion

3.1. Field-dependent ac susceptibility

3.1.1. General features. Before discussing the general features of $\chi_{ac}(H, T)$ it is appropriate to review briefly the results of the high-field magnetoresistance measurements reported recently [22], more particularly the spontaneous resistive anisotropy (SRA), as these results were instrumental in initiating the present study. The SRA is defined as:

$$\frac{\Delta\rho}{\rho_0} = \left[\frac{\rho_\parallel(B) - \rho_\perp(B)}{\rho_0}\right]_{B\to 0} \tag{1}$$

a ratio which specifies the difference between the longitudinal ($\rho_\parallel$) and transverse ($\rho_\perp$) magnetoresistance of a (technically) single domain ferromagnetic system extrapolated to zero induction (B); roughly the transport equivalent of the spontaneous magnetization.

A non-zero value for the SRA relies on the presence of both a polarizing field and spin–orbit coupling at scattering sites [30]. The measured SRA in CuNi was shown [22] to display the same percolation related, power law dependence on reduced composition as reported [15] for PdNi, *viz*:

$$\frac{\Delta\rho}{\rho_0} \propto \left(\frac{c - c_0}{c_0}\right)^{\Delta} \tag{2}$$

in which the 'exponent' Δ ($\simeq 9/4$) also assumes the same value as in PdNi [15], while c_0 (the critical concentration for the emergence of ferromagnetism at $T = 0$) was estimated at 44.5 at.% Ni (in Cu). More important, the technique by which the SRA was measured for compositions close to c_0 involved the application of external fields as low as 0.5 mT. The appearance of an SRA in such low *applied* fields provides convincing support for the premise, as argued originally for PdNi, that the relevant polarising field is the *exchange* field [15], so that such measurements indicate that ferromagnetic order exists at finite temperature for compositions as low as 45 at.% Ni (at least over distances comparable to a conduction electron mean free path).

Figure 1 reproduces a survey of the zero-field ac susceptibility $\chi(0, T)$ of eight samples with compositions ranging from 45 to 54 at.% Ni. The demagnetizing factors for these samples were estimated, typically, to be $N \sim 10^{-5}$ (when $\chi(0, T)$ is the susceptibility per unit mass), around 100 times smaller than that for a sphere. This choice was deliberately made as comparisons with previously studied systems, such as NiMn [31] and amorphous FeMn [32], revealed that limiting the measured response unnecessarily (by setting low values for N^{-1}) can lead to erroneous conclusions.

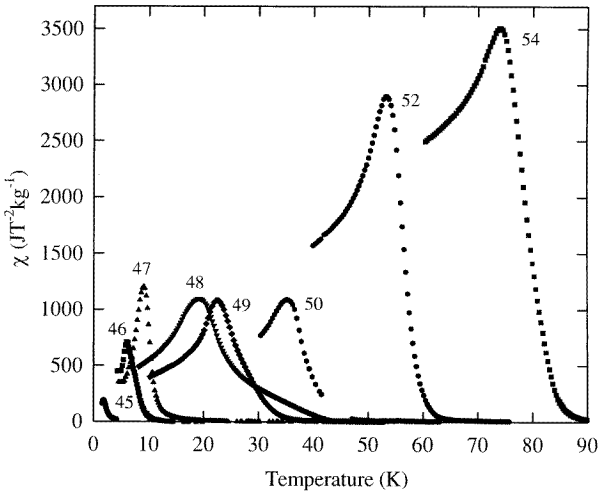

Figure 1. The zero-field susceptibility of selected CuNi samples; the Ni composition (in atomic %) is shown against the appropriate data.

The overall features and the general shape of the temperature dependence of the data displayed in figure 1 show considerable similarity as a function of Ni composition. At 54 at.% Ni—generally agreed to be a well defined ferromagnet [21]—$\chi(0, T)$ increases rapidly with increasing temperature below 100 K as the Curie temperature T_C is approached from above, it peaks just below T_C at the Hopkinson or principal maximum [25, 26] (designated by the temperature T_H) and falls on further cooling to a value of roughly one

half of this maximum some 20 K ($T \sim 3/4T_C$) below the peak. The Hopkinson maximum is *not* critical in origin, but results from processes associated with the regular/technical contributions to the susceptibility [33]. The specific choice of sample geometry adopted here emphasizes this result; the value of $\chi_{ac}(0, T_H)$ observed for the 54 at.% Ni sample is less than *one-tenth* of the limit set by N^{-1}. Furthermore, the use of small-N samples means that, for a given H_a, in order to reach the demagnetization limit (at which the internal field ($H_i = H_a - NM$, in the usual notation) is zero) in an ac measurement, the magnetization must oscillate (reverse) with ever increasing amplitude as N is decreased. Under such circumstances one is much more likely to observe the influence of any process (such as anisotropy) which pins the response, than in large-N samples [25, 26, 34]. Here we suggest that one major contribution to the anisotropy is single ion (Ni) spin–orbit coupling, the presence of which is an essential ingredient for the observation of the SRA, mentioned above. For the other samples surveyed in this figure, two features warrant comment; first, the susceptibility peak amplitudes do not fall monotonically with decreasing Ni concentration, and will be discussed in more detail below, and second, the apparent sharpening of this zero-field response below 48 at.% Ni is due principally to the decrease in T_C, so that the features mentioned above for the 54 at.% Ni sample are now compressed into a rapidly diminishing temperature interval.

The non-monotonic variation of $\chi(0, T_H)$ with Ni concentration c is reproduced in figure 2. From this figure it can be seen that the amplitude of this principal (Hopkinson) maximum *increases* initially as c falls from 55 to 54 at.% and then declines by a factor of about three as c is decreased to 50 at.%. Between 50 and ~46 at.% $\chi(0, T_H)$ passes through a plateau region, before declining sharply at 45 at.% Ni as c_0 is approached from above. The inset in this figure reproduces the corresponding data [35] for Ni in Pd, which are remarkably similar; here, though, the critical concentration is near 2.3 at.% Ni and the Hopkinson maxima $\chi(0, T_H)$ scale roughly as the ratio of the Ni concentrations in the two systems. Such similarities suggest related magnetic structures.

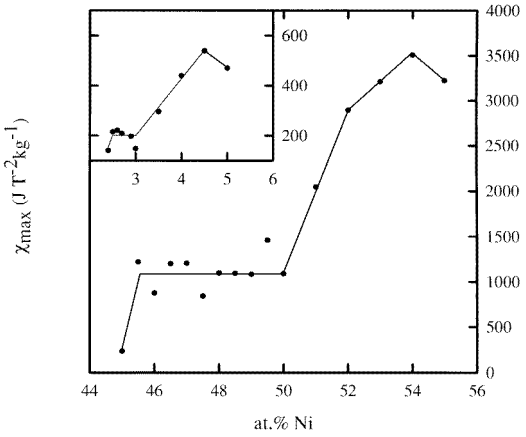

Figure 2. The height of the principal (Hopkinson) maxima, taken from data similar to those shown in figure 1, plotted against the Ni concentration for the CuNi system. The inset shows similar data for PdNi.

The effects of small superimposed static biasing fields H_a, investigated in detail for the first time for this system, are summarized in figures 3, 8 and 10 for three representative samples containing 54, 49.5 and 46 at.% Ni respectively. As reported for a variety of other

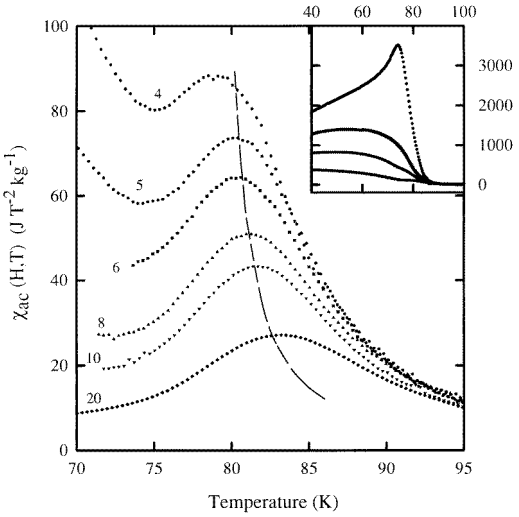

Figure 3. The field-dependent ac susceptibility $\chi(H, T)$ (in J T^{-2} kg^{-1}) (corrected for background and demagnetizing effects) of the 54 at.% Ni sample plotted against temperature; the numbers marked against each curve indicate the superimposed static biasing field (in mT). The dashed line represents the predicted location of the cross-over line (equation (4)) using Heisenberg model exponents. The inset shows the behaviour of the zero-field response along with the effects of small static biasing fields of 0.5, 1 and 2 mT in which the critical peak structure is not resolved.

ferromagnetic systems [26, 32, 34] these latter fields suppress the Hopkinson maximum in both amplitude and temperature, thus enabling secondary, critical peaks to be observed. These critical peaks decrease in amplitude and move upward in temperature above T_C as the field increases in agreement with the predictions of the static scaling law [26, 32, 34]. The locus of these critical maxima defines the cross-over line [36] (above which the response is thermally dominated, as opposed to being field dominated below it), the origin of which can be understood on the basis of the fluctuation—dissipation theorem [36]. The observation of such behaviour is indicative of critical fluctuations accompanying a (continuous) paramagnetic to ferromagnetic phase transition [26]. A quantitative analysis of such data proceeds by writing the singular/critical contribution to the susceptibility $\chi(h, t)$ in the vicinity of such a transition as [37]

$$\chi(h, t) = t^{-\gamma} F(h/t^{\gamma+\beta}) = h^{1-1/\delta} G(h/t^{\gamma+\beta}) \tag{3}$$

where $h \sim H_i/T_C$ and t $(=|T - T_C|/T_C)$ are conventional linear scaling fields. The latter predicts the peak temperature T_m to increase with field according to

$$t_m = \frac{T_m - T_C}{T_C} \propto H_i^{1/(\gamma+\beta)} \tag{4}$$

a relationship which defines the cross-over line (with $(\gamma + \beta)$ being the cross-over exponent) while the peak amplitude should decrease (for $\delta > 1$) as

$$\chi(H_i, T_m) \propto H_i^{1/\delta - 1} \tag{5}$$

(i.e. with the *same* exponent as the field dependence of the susceptibility *along* the critical isotherm, although (5) is advantageous as it does *not* require this isotherm (i.e. T_C) to be identified). The predictions of (4) and (5) are clearly in qualitative agreement with the data in figures 3 to 5; a quantitative comparison is carried out below.

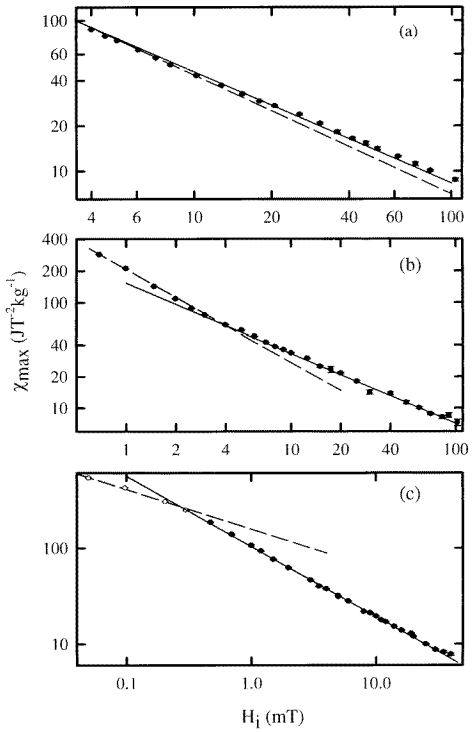

Figure 4. The height of the (critical) susceptibility maxima, χ_{max} (in J T^{-2} kg^{-1}), taken from data similar to those shown in figure 3, plotted against the estimated internal field (in mT) on a double logarithmic scale for Ni compositions of (a) 54 at.%, (b) 49.5 at.% and (c) 46 at.% Ni. The full and dashed lines yield the effective exponent estimates discussed in the text using the power law relationship expressed in equation (5). In (c) the open symbols are discussed in the main body of this paper, section 3.1.2(c).

3.1.2. Quantitative estimates. One pre-requisite for meaningful fits of (4) and (5) to experimental data is obviously that the *measured* response be dominated by that component arising from critical fluctuations, on which these equations are based. In practice this condition is met in materials with a rather low net moment in which the non-critical or regular contribution (from, for example, domain wall motion and/or coherent rotation) is driven to (technical) saturation in quite low fields. Such behaviour generally results in a rapid suppression of the Hopkinson maximum in both amplitude and temperature. This does not occur here. Fields in excess of several mT need to be applied before critical peak structure can be resolved; such fields are close to two orders of magnitude larger than those necessary to reveal critical structure in the field-dependent susceptibility of the softest materials (i.e. PdFe [38]). Furthermore, even with critical peak structure resolved it is not clear that the regular contribution to the peak amplitude is negligible (the temperature derivative of the measured response reverses sign rapidly as the temperature is lowered in contrast to model calculations in which $\chi(H, T)$ declines monotonically below the critical peak [26, 39]), thus complicating detailed analysis, as confirmed below. Consequently, while an orbital component in the total Ni moment is an essential ingredient for the observation of an SRA (from which a reliable estimate for c_0 can be made [15, 22]), the associated

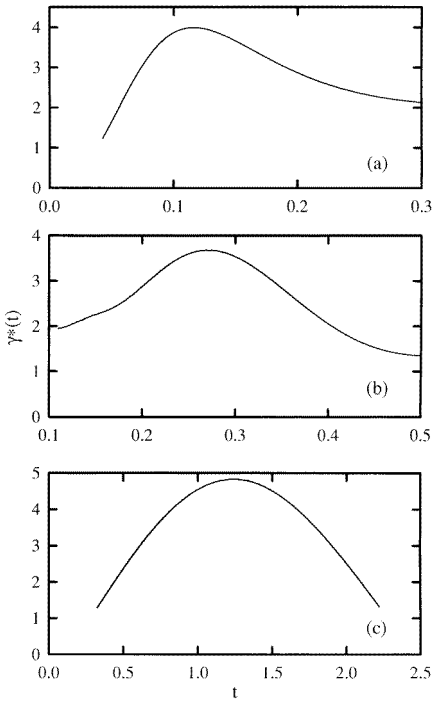

Figure 5. The temperature dependence of the effective Kouvel–Fisher susceptibility exponent $\gamma^*(T)$ (defined in equation (6)) plotted against the reduced temperature t for samples containing (a) 54 at.% Ni, (b) 49.5 at.% Ni and (c) 46 at.% Ni.

(magnetic) hardness/anisotropy complicates the interpretation of $\chi(H, T)$ data. In terms of the effects of the latter, three concentration regimes appear to exist.

(a) $c \geqslant 52$ *at.% Ni.* This is the concentration region with the largest values for the susceptibility near the Hopkinson maximum, $\chi(0, T_H)$, figure 2. For these samples applied fields of typically 4 mT are required to first resolve critical peak structure, as shown in figure 3; the amplitude of the Hopkinson maximum remains significant for fields in which critical structure is first resolved (the inset in this figure), so that the measured response (shown in the main body of this figure) probably contains a significant regular contribution, particularly for $\mu_0 H_a \leqslant 10$ mT. A first estimate for T_C is made by plotting the temperature T_m of the critical maxima, evident in figure 3, against $H_i^{1/(\gamma+\beta)}$ (i.e. $H_i^{0.57}$ assuming localized Heisenberg model [40] exponent values), and fitting to a straight line, the intercept of which gives the required estimate. Examples of such plots have been given previously [26, 34] and are not reproduced here, especially as such estimates are refined (through small adjustments ΔT_C in T_C ($\Delta T_C/T_C \leqslant 10^{-2}$)) to produce a consistent set of plots of the type discussed below [26, 38].

The exponent δ of equation (5) is estimated generally through double logarithmic plots of the height of the maxima shown in figure 3 (corrected for background and demagnetizing effects) against the calculated internal field [26] $\mu_0 H_i$, figure 4(a). This exponent estimate is independent of the choice for T_C. For the 54 at.% Ni sample, as shown in figure 4(a), these data are essentially linear (confirming the power law relationship of (5)) and indicate

that a single value of $\delta^* = 4.2(1)$ provides a reasonable characterization of such data over the field range $4 \leqslant \mu_0 H_i \leqslant 100$ mT. This plot warrants two further comments. First, the scaling law, (3), is valid in the limit $h \to 0$ ($H_i \to 0$) and $t \to 0$ ($T \to T_C$), so that the inability to resolve critical peak structure below 4 mT means that the true asymptotic limit cannot be accessed; thus *effective* exponents (δ^*) alone are quoted. Second, *effective* exponent values which change away from the critical point (i.e. with increasing h and/or t) are well documented [26, 41] in systems with exchange coupling strength disorder (i.e., a finite variance in the distribution characterizing the latter); in the present context values for $\delta^*(H_i)$ which decrease with increasing H_i have been reported experimentally for a number of systems with such disorder [26], and are also reproduced by model calculations [26, 39]. Close examination of figure 4(a) does reveal a small amount of curvature at lower fields ($\mu_0 H_i \leqslant 10$ mT), from which a value of $\delta^* \simeq 4.8$—the isotropic, localized 3D Heisenberg near neighbour model value—may not be inappropriate. Considering the comments made above, however, such a result cannot be taken as confirming a Heisenberg model value for δ in this system, merely that these data *may* be consistent with this value (and adding further support to a localized model interpretation of this system).

The behaviours for the remaining exponents are summarized in figures 5, 6 and 7. The first of these shows the temperature dependence of the effective Kouvel–Fisher susceptibility

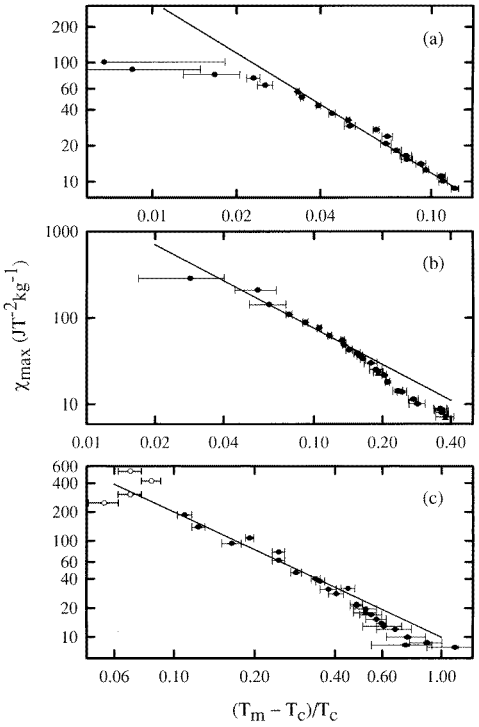

Figure 6. The (critical) susceptibility peak amplitude χ_{max} (in J T^{-2} kg^{-1}) (corrected for background and demagnetizing effects) plotted against the reduced susceptibility peak temperature on a double logarithmic scale using the T_C values listed in table 1. The lines drawn yield the susceptibility exponent values, shown in the same table, obtained from data closest to T_C through the use of the power law relation expressed in equation (7).

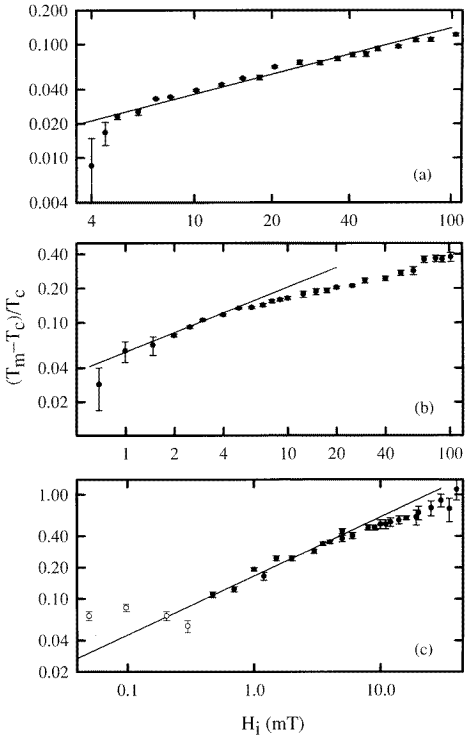

Figure 7. The reduced susceptibility peak temperature plotted against the estimated internal field (in mT) on a double logarithmic scale. The lines drawn represent the power law relationship summarized by equation (4) for the cross-over line with Heisenberg model exponents. These data are for samples with Ni concentrations of (a) 54 at.%, (b) 49.5 at.% and (c) 46 at.%.

exponent [42]

$$\gamma^*(T) = -\mathrm{d}\ln(\chi(0,t))/\mathrm{d}\ln(t) \tag{6}$$

obtained from the zero-field susceptibility. The temperature dependence shown by the latter in figure 5(a)—specifically the maximum in $\gamma^*(T)$ ($\sim$4) near $t \sim 0.1$ prior to a decline towards a mean field value of 1 at higher temperature—is characteristic of systems with exchange bond disorder [41]. The effects of anisotropy are clearly evident in this figure where, for $t \leqslant 0.05$, $\gamma^*(T)$ falls rapidly to values less than 1 due to the failure of $\chi(0,t)$ to approach the demagnetization factor limit (N^{-1}); clearly near this latter temperature estimates of $\gamma^*(T)$ from (6) are unreliable (due—we suggest—to the influence of coercive effects), and this exponent is obtained from the relationship between $\chi(h,t_m)$ and t_m (i.e. from (4) and (5), assuming the validity of the Widom relation $\gamma = \beta(\delta - 1)$)

$$\chi(h,t_m) \propto t_m^{-\gamma}. \tag{7}$$

These data are summarized in figure 6(a), where the solid line drawn corresponds to the Heisenberg model value [40] of $\gamma = 1.386$. Figure 7(a) summarizes the applicability of the power law relationship (5), and the line drawn again corresponds to localized 3D Heisenberg model values for the cross-over exponent $(\gamma + \beta)^{-1} = 0.57$. These last three figures were based on a final value of $T_C = 78.4$ K for this sample, corresponding approximately to the inflexion point on the zero-field curve; the values for T_C, along with various effective exponent estimates, are summarized in table 1.

Table 1. Summary of parameters deduced from the field-dependent ac susceptibility of CuNi samples. The (reduced) temperature and field range following each effective exponent estimate indicates the corresponding range over which that estimate was made.

at.% Ni	T_C (K)	γ^*	t	$\gamma^*+\beta^*$	$\mu_0 H_i$ (mT)	δ^*_{LF}	$\mu_0 H_i$ (mT)	δ^*_{HF}	$\mu_0 H_i$ (mT)
45.0	1.7 (3)	1.00 (5)	0.1–1.0	1.75 (3)	0.5–40	1.47 (2)	0.1–0.8	3.00 (1)	1–85
45.5	4.2 (1)	1.39 (10)	0.06–1.3	2.0 (1)	1.5–15	2.00 (4)	0.1–0.5	3.00 (2)	1.5–100
46.0	5.6 (1)	1.39 (10)	0.06–0.4	1.75(20)	0.2–8	1.69 (2)	0.04–0.3	3.70 (5)	0.3–40
46.5	8.1 (2)	1.39 (20)	0.15–0.4	1.75 (30)	2.5–10	5.8 (2)	1.5–7	3.56 (5)	2–50
47.0	9.8 (2)	1.39 (10)	0.08–0.4	1.75(20)	1–35	4.8 (3)	0.5–4	3.8 (1)	0.7–100
47.5	13.1 (3)	1.39 (10)	0.08–0.3	1.75 (20)	1.5–18	12 (1)	1.5–4	3.7 (1)	3–100
48.0	20.1 (4)	1.20 (10)	0.04–0.5	1.75 (20)	1.5–15	8.6 (6)	1.5–4	2.13 (2)	4–100
48.5	22.2 (6)	1.39 (20)	0.04–0.2	1.75 (10)	1.5–12	<0	1.5–6	3.73 (5)	5–100
49.0	25.1 (6)	1.39 (20)	0.09–0.2	1.75 (10)	1.5–10	<0	1.5–5	3.0 (1)	4–100
49.5	29.4 (6)	1.39 (10)	0.03–0.16	1.75 (20)	0.7–5	8.4 (3)	0.6–4	3.0 (1)	3–100
50.0	33.3 (7)	1.39 (10)	0.04–0.2	1.75 (30)	1–10	10.2 (4)	1–5	3.0 (1)	4–100
51.0	39.1 (8)	1.39 (20)	0.06–0.25	1.75 (30)	2–70	4.80 (6)	1–3	2.00 (2)	3–100
52.0	55.4 (11)	1.39 (5)	0.03–0.17	1.75 (7)	4–100	—	—	3.18 (3)	3–100
53.0	62.8 (13)	1.39 (10)	0.03–0.15	1.75 (20)	5–30	—	—	4.2 (2)	3–100
54.0	78.4 (20)	1.39 (6)	0.03–0.15	1.75 (10)	5–70	4.80 (15)	3.5–10	4.17 (5)	3.5–100
55.0	83.2 (20)	1.39 (10)	0.02–0.11	1.75 (20)	6–100	4.80 (20)	4–8	3.25 (9)	4–100

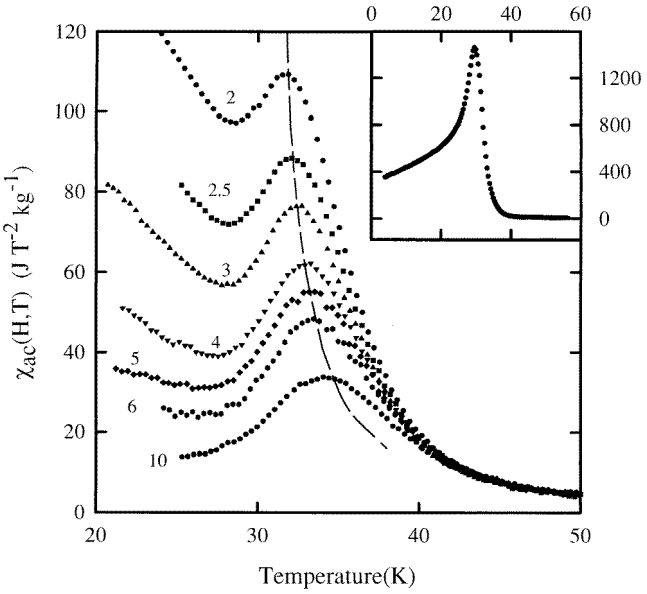

Figure 8. As in figure 3, but for the 49.5 at.% Ni sample.

(b) $48 \leqslant c \leqslant 51$ *at.% Ni.* This is essentially the plateau region in figure 2. In these samples the effects of anisotropy near the transition appear relatively suppressed as critical peak structure is now revealed in applied fields of around 1 mT (figure 8). This result prevails despite the observation that the zero-field response displays a sharper Hopkinson maximum (inset figure 8) and the coercive field $\mu_0 H_c$ (estimated from 'butterfly loops' at 4.2 K, i.e., plots of $\chi(H_a, 4.2\ \mathrm{K})$ against H_a) shows no significant change with composition in this range (figure 9).

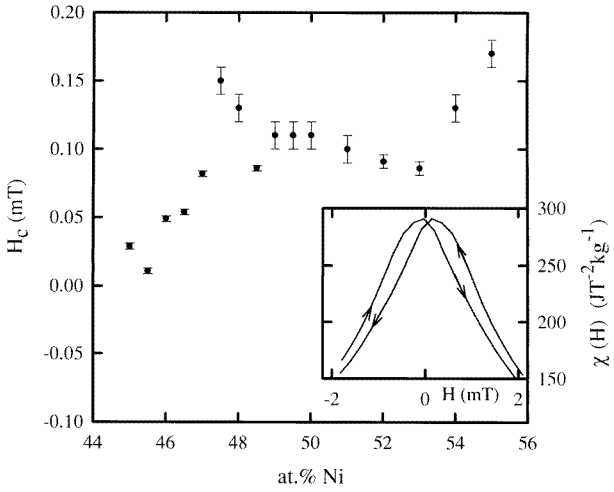

Figure 9. The coercive field $\mu_0 H_c$ (in mT) plotted against Ni concentration (in at.%). These fields were measured at 4.2 K except for the two samples of lowest composition, for which measurements were carried out at 1.5 K. The inset shows a butterfly loop—the splitting of which yields H_c—for the 49.5 at.% sample.

Various effective exponent estimates are made in figures 4(b), 5(b), 6(b) and 7(b). Figure 5(b) confirms the general behaviour expected [41] of the effective susceptibility exponent (6) in systems with exchange bond disorder (although the detailed features are clearly different from those exhibited by the 54 at.% Ni sample); figure 6(b) also provides an estimate for this exponent using (7) which is, in our opinion, more reliable as $t \rightarrow 0$ due to the presence of significant anisotropy, as discussed above. Figure 7(b) reproduces the behaviour for the cross-over exponent. These latter three figures all show clearly the increases in both $\gamma^*(t)$ and $\beta^*(t)$ expected [39, 41, 42] as t increases in bond disordered systems; specifically figure 5(b) displays the maximum in $\gamma^*(t)$ near $t \leqslant 0.3$ directly while the deviations evident in figures 6(b) and 7(b) illustrate these effects indirectly. That such deviations in effective exponent values become more marked in this concentration range is consistent with trends predicted by models assuming a Gaussian distribution of exchange coupling strength [26, 39, 42] in which the ratio (η) of first (J_0) to second moment (J) decreases as the concentration c falls towards the critical composition c_0.

The most significant changes, however, appear in the behaviour of δ^*. As can be seen in figure 4(b), in this sample critical peaks can be resolved in applied fields as low as 0.7 mT, and the predicted [26, 39, 42] increase in $\delta^*(H)$ with decreasing field is observed. Such agreement between measurement and model prediction is, however, only partial; whereas the high-field slope drawn through the data in figure 4(b) corresponds to a near mean field value of $\delta^* \simeq 3$, the low-field slope yields $\delta^* \geqslant 8$, far in excess of 3D Heisenberg model values, a result most likely attributable to the presence of a substantial regular contribution to the measured response in this regime (so that the measured peak susceptibility is *not* dominated by the critical component in these low fields). Large effective δ^* values—well in excess of localized 3D Heisenberg model predictions—have been reported previously for the PdGd system [43].

As a final comment on the behaviour of $\chi(H, T)$ in this concentration regime, it should be noted that the final T_C values (table 1) fall progressively below the inflection point on the zero-field curve and approach the principal/Hopkinson maximum (T_H).

(c) $c_0 \leqslant c \leqslant 47$ *at.% Ni.* In this regime the approach of T_C to T_H continues even as the value for $\chi(0, T_H)$—figure 2—falls rapidly as c approaches the critical concentration from above. Figure 10 shows $\chi(H, T)$ for the 46 at.% Ni sample for applied fields below 0.7 mT; in this composition range only one such peak is visible for all available values of the static external biasing field H_a. At *low* applied field, this peak decreases in amplitude but remains at essentially the same temperature as H_a increases; however, above typically $\mu_0 H_a \simeq 1$ mT, these peaks move *upwards* in temperature as H_a increases, in qualitative agreement with the behaviour predicted by the scaling law.

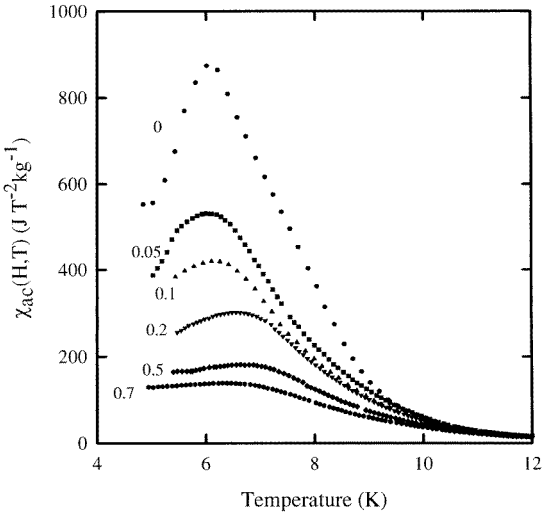

Figure 10. As in figure 3, for the 46 at.% Ni specimen.

The results of quantitative comparisons with the scaling law predictions, (4)–(7), are reproduced in figures 4(c), 5(c), 6(c) and 7(c). The effective Kouvel–Fisher susceptibility exponent $\gamma^*(t)$ is shown in figure 5(c), from which it can be seen that the peak in this effective exponent now occurs beyond $t = 1$. Nevertheless the (preferred) estimate based on the use of (7) yields $\gamma^*(t)$ consistent with the 3D Heisenberg model value for $0.07 \leqslant t_m < 0.4$, figure 6(c), while figure 7(c) suggests consistency with Heisenberg model values for the cross-over exponent for $0.2 \leqslant \mu_0 H_i \leqslant 6$ mT. In both of these latter figures the open symbols refer to the field regime where the peak temperature (figure 10) is *not* changing with field.

The behaviour of $\delta^*(H)$ is also anomalous for these samples with $c_0 \leqslant c \leqslant 47$ at.% Ni. Figure 4(c) indicates that while δ^* ($\mu_0 H_i \geqslant 0.4$ mT) ≈ 3.7 (intermediate between 3D Heisenberg and mean-field model values, as expected at 'higher' fields in the presence of bond disorder), the *low* field value for δ^* actually *declines* ($\delta^* \sim 1.7$ for $\mu_0 H_i < 0.4$ mT). The latter is clearly related to the apparent evolution of the critical peak structure from the vicinity of the principal/Hopkinson maximum in this concentration range, so that despite the resolution of the peak structure in fields $\leqslant$0.2 mT here (as $H_c \to 0$ for $c \to c_0$, figure 9), this principal maximum is itself diminishing rapidly in amplitude as $c \to c_0$ (figures 1 and 2).

Thus, despite the presence of anisotropy in the CuNi system which precludes both a rapid suppression of the technical/regular components in the measured response by applied fields and hence an evaluation of the true asymptotic ($h \to 0$, $t \to 0$) critical behaviour, the

overall picture emerging, as summarized in table 1, is that this critical behaviour is likely describable by 3D Heisenberg model exponents (some irregularities notwithstanding), thus supporting a localized model picture for the behaviour of this system. This is true down to 45 at.% Ni (the lowest concentration studied), consistent with the estimate of $c_0 \simeq 44.5$ at.% Ni deduced from the detailed analysis [15] of the SRA. Despite the much weakened response at 45 at.% Ni (here the Hopkinson maximum is just 5% of that measured in the 55 at.% sample), it displays a critical peak structure similar to that shown in figure 10 for the 46 at.% specimen, and a summary of the analysis of this structure is presented in figures 11–13. The latter indicate a marked shift towards mean field exponents (the 'best fit' value for γ^* in figure 11 is closer to 1 rather than 1.39, and the higher-field value for δ^* is 3.0) at this lowest composition studied, which probably reflects the proximity of this latter concentration to the estimated c_0 [22].

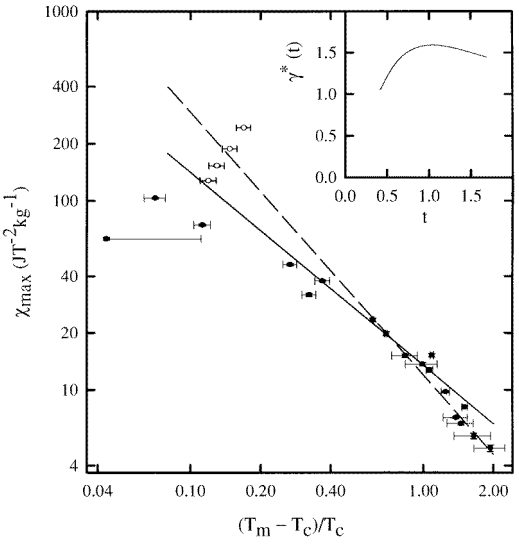

Figure 11. The (critical) susceptibility peak amplitude χ_{max} (in J T^{-2} kg^{-1}) plotted against the reduced peak temperature, as in figure 6, for the 45 at.% sample. Here the dashed line represents the Heisenberg model value of $\gamma = 1.39$, while the solid line, a 'best fit', with $\gamma = 1.0$. The inset shows the temperature variation of the effective Kouvel–Fisher exponent.

3.2. Transport measurements

The conclusions reached regarding the critical composition, c_0, for the appearance of ferromagnetism in the present CuNi samples from a detailed analysis of both the spontaneous resistive anisotropy (SRA) (reported previously [22]) and the field- and temperature-dependent ac susceptibility are confirmed by the transport measurements summarized below. The latter include the zero-field resistivity $\rho(T)$ and, for the first time, the low-field resistive anisotropy (LFRA) defined by the ratio

$$\frac{\Delta\rho(H_a, T)}{\rho(T)} = \frac{\rho_{\parallel}(H_a, T) - \rho_{\perp}(H_a, T)}{\rho(0, T)} \tag{8}$$

measured in an applied field of $\mu_0 H_a = 10$ mT (the latter is too weak to affect appreciably the intrinsic spin polarization or the conduction electron trajectories at the temperatures

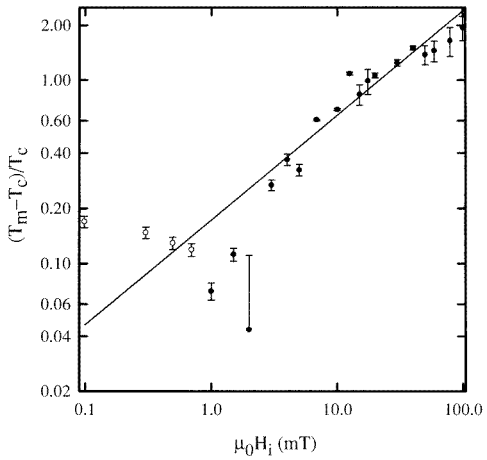

Figure 12. As in figure 7, for the 45 at.% Ni sample.

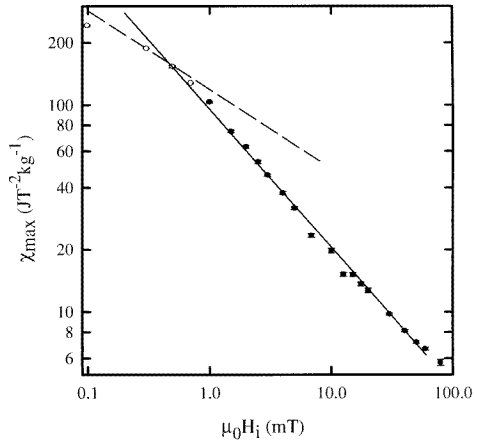

Figure 13. As in figure 4, for the 45 at.% Ni specimen.

of interest; its role is to provide a preferred/reference direction for spin–orbit coupling by establishing a single domain structure over length scales comparable to the electronic mean free path [15, 44]). Both $\rho(T)$ and the LFRA were measured using the relative difference ac method [15, 44]; here, having measured the voltage drop V_0 across the sample at some predetermined initial temperature, the voltage *change* $\Delta V(H_a)$ induced by the rotation of a small applied field ($\mu_0 H_a \simeq 10$ mT) from a parallel to a perpendicular orientation, and the subsequent change $\Delta V(T)$ (with $H_a = 0$) accompanying a small temperature increase ΔT, are estimated with high precision. By the simple addition of the changes of the latter type, $V_0(T)$ $(=V_0 + \sum \Delta V(T))$ can be found and the corresponding resistivity $\rho(T)$ estimated by knowing the sample current and the conventional form factor; more importantly, the (small) LFRA can be calculated directly from the ratio $\Delta V(H_a)/V_0(T)$, thus avoiding both current and form factor uncertainties. Typical data obtained in this way (for the 49.5 at.% Ni sample) are reproduced in figures 14 and 15. From figure 14 it can be seen that $\rho(T)$ displays the characteristic 'knee' near T_C, indicating the onset of a reduction

in the spin-disorder scattering accompanying the establishment of an ordered phase at a paramagnetic to ferromagnetic transition. A quantitative estimate for the latter temperature can be found [45] from the derivative $\mathrm{d}\rho/\mathrm{d}T$; here this derivative is calculated directly from the data using a point-to-point difference method (i.e. from $\Delta V(T)/\Delta T$), and the results are shown in the inset in figure 14.

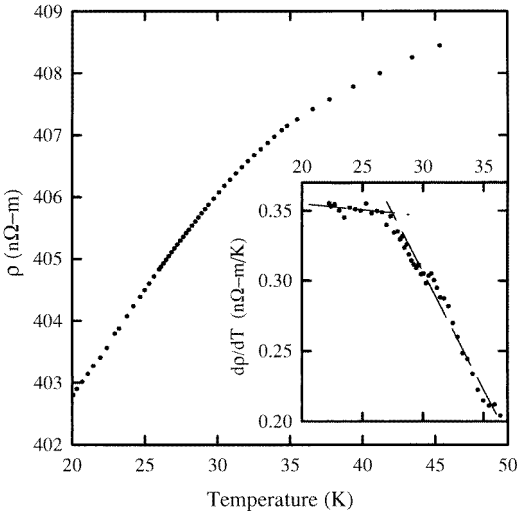

Figure 14. The temperature dependence of the zero-field resistivity $\rho(T)$ (in nΩ m) for the sample with a Ni concentration of 49.5 at.%. The inset shows the derivative data $\mathrm{d}\rho/\mathrm{d}T$, and the intersections of the lines drawn yield the T_C estimate listed in table 2.

The derivative data reproduced in this inset exhibit the scatter characteristic of point-to-point methods; nevertheless, we find that $\mathrm{d}\rho/\mathrm{d}T$ consists of a plateau regime immediately below T_C followed by the onset of a rapid decline (as reported previously [45] for a similarly prepared 48.2 at.% Ni sample), rather than a well defined maximum in this derivative which defines T_C in some site disordered magnetic systems [45]. Thus T_C is taken as the onset of this rapid decline in $\mathrm{d}\rho/\mathrm{d}T$, when the simple linear interpolation shown by the dashed lines in this inset provide an appropriate estimate for T_C (listed in table 2). Here this latter is as reliable as other methods in which $\rho(T)$ is fitted to an arbitrary function (such as a polynomial of low degree, the coefficients of which are determined by some least-squares criterion) over a sliding temperature interval, and then generating $\mathrm{d}\rho/\mathrm{d}T$ analytically from the fitted function.

Before comparing these T_C estimates from $\rho(T)$ with those found from $\chi(H,T)$, the LFRA data will be presented. Figure 15 shows such data for the same 49.5 at.% Ni sample. The LFRA data in CuNi appear to display the effects of short-range order immediately above T_C in a manner more marked than any of the other measurements that have been reported here. In other systems in which the LFRA has been measured recently [44], this ratio falls to zero at T_C, being represented typically by the form [44]:

$$\begin{aligned} \frac{\Delta\rho(H_a,T)}{\rho(T)} &= A(\eta)\left(\frac{T_C-T}{T_C}\right) \qquad && 0.7T_C \leqslant T \leqslant T_C \\ &= 0 && T > T_C. \end{aligned} \tag{9}$$

Table 2. Summary of parameters deduced from transport measurements.

at.% Ni	T_C (K): LFRA	$A(\eta)$ (10^{-3})	T_C (K): $\rho(T)$
45.0	3.8 (10)	0.07	<2
45.5	5.6 (10)	0.17	<4.2
46.0	8.2 (5)	0.30	7.2 (5)
46.5	10.4 (7)	0.43	9.3 (5)
47.0	10.5 (6)	0.44	10.3 (5)
47.5	14.6 (10)	0.63	11.9 (10)
48.0	20.2 (8)	0.96	19.6 (5)
48.5	23.9 (8)	1.11	22.4 (6)
49.0	24.8 (9)	1.14	23.0 (5)
49.5	30.4 (9)	1.43	28.8 (6)
50.0	33.4 (10)	1.58	31.5 (7)
51.0	40.4 (10)	2.17	40.6 (7)
52.0	57.9 (10)	2.46	55.0 (8)
53.0	67.6 (10)	3.60	68.3 (8)
54.0	84.8 (10)	3.62	82.5 (8)
55.0	86.0 (10)	4.59	83.1 (8)

This latter result is reproduced (again) by localized models [30, 44] in which the *anisotropy* arises principally from local *electric quadrupole* scattering (the lowest contributing term in a multipole expansion of the nonspherical charge distribution, hence the requirement of a non-zero orbital angular momentum), when

$$\frac{\Delta\rho}{\rho} \simeq \left(\frac{D}{V}\right)[\langle S_Z^2\rangle - S(S+1)/3]. \tag{10}$$

Here the term in square brackets reflects the quadrupolar origin of the anisotropy (displaying the $(3\cos^2\theta - 1)$ angular dependence expected of quadrupolar effects with axial symmetry about the applied magnetic field direction [30]), D characterizes the local electric quadrupole moment while V ($\gg D$) represents the screened Coulomb potential (essentially arising from the valence difference between host and dopant sites in localized models; this 'electric monopole' contribution to the scattering can dominate the resistivity in amorphous and strongly disordered systems: indeed, figure 14 shows that $\rho(T)$ changes by less than 1% from 0.7 T_C to T_C in the 49.5 at.% Ni sample). The *ratio* in (10) is, of course, independent of *other* band structure details, which contribute equivalently to numerator and denominator.

The data reproduced in figure 15 are unusual in that they display a significant high-temperature 'tail', indicating that this ratio does not become zero at T_C in this system. Spin–spin correlations, resulting in a non-zero LFRA, might be expected immediately above T_C; such correlations could arise from either critical scattering (associated with a correlation length $\xi(T)$ which decreases with increasing temperature above T_C, but within which the quadrupolar operator, $\langle S_Z^2\rangle - S(S+1)/3$, is not zero) or from short-range statistical fluctuations in the Ni site occupation, or a combination of both. The second possibility seems more likely here due to both a failure to observe the effects of a finite correlation length above T_C in other systems [44] and the documented clustering tendencies of the CuNi system (discussed in more detail below). Irrespective of the origin of this 'tail', its effects have been accounted for using the technique illustrated in figure 15. From the latter it is clear that the present data also display the expected linear temperature dependence below T_C, while the 'tail' regime above T_C has also been approximated (in first order) by a linear temperature variation; the intersection of the two lines drawn yields an estimate

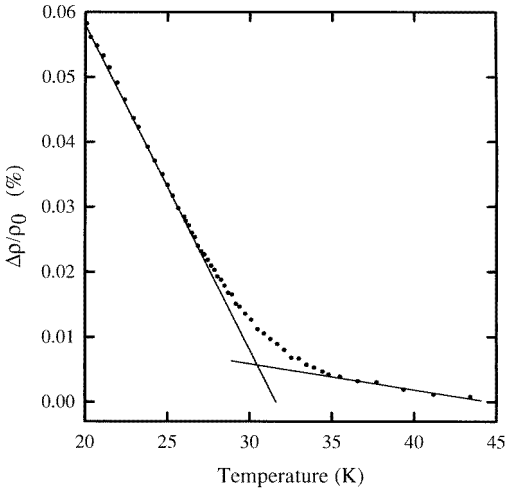

Figure 15. The LFRA, defined in section 3.2, equation (8), plotted against temperature for the 49.5 at.% Ni sample. The two solid lines are discussed in the text; their intersection yield the T_C estimate listed in table 2.

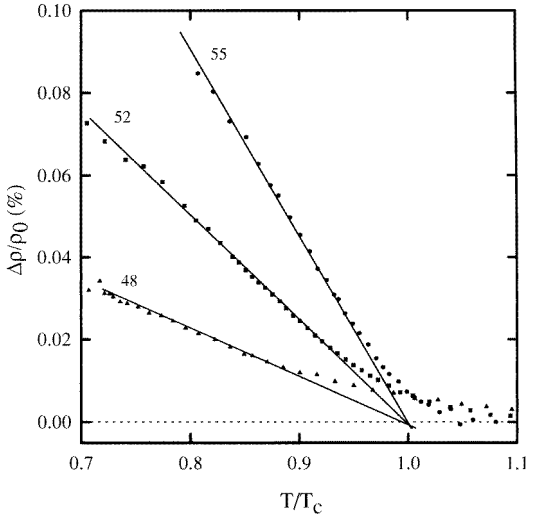

Figure 16. The LFRA data plotted against reduced temperature for three representative specimens with Ni concentration (in at.%) marked against the appropriate data. The slope of the lines drawn provide estimates of the coefficient A in equation (9), as listed in table 2.

for T_C from these LFRA data. Such estimates are also summarized in table 2. Figure 16 then reproduces a representative selection of LFRA data plotted as a function of reduced temperature (T/T_C) using the T_C values estimated above. The principal aim of this figure is to illustrate the second prediction of localized models contained in (9), that is, the exchange bond dependence of the coefficient $A(\eta)$ in the equation, corresponding to the slope of the linear dependence in the LFRA below T_C. Model predictions indicate that $A(\eta)$ should

increase as η $(=J_0/J)$ increases [44], a prediction consistent with the observed behaviour resulting, for example, from the introduction of hydrogen into amorphous FeZr [44]. The data reproduced in figure 16 and the estimates for A shown in table 2 are qualitatively consistent with localized model approaches in which η increases (a decrease in the relative amount of bond *disorder*) as the Ni concentration increases above c_0.

Finally we comment on a comparison of the estimates of T_C obtained from the three properties examined here. Overall there is reasonable agreement between these various estimates within the listed uncertainties; the latter substantial in all three measurements, due to a significant regular contribution in $\chi(H, T)$, an unconventional behaviour in $\mathrm{d}\rho/\mathrm{d}T$ and a marked tail in the LFRA, all of which have been discussed above. Furthermore, while the magnetic and transport measurements were made on samples cut from adjacent sections of the same cold-rolled strips, the possibility might still exist that some inhomogeneity persisted in the initial strips, and despite being annealed together, samples of different size might suffer (slightly) different quenching rates. While an investigation of some of these points is presented below, it should be stressed that the resistivity and LFRA measurements were performed on the *same* sample essentially simultaneously (and certainly with the same thermometry); the spread in T_C values derived from these latter measurements is no greater than that between either of these estimates individually and that deduced from $\chi(H, T)$. Nevertheless, conclusive evidence supporting the existence of ferromagnetism in samples of the lowest concentrations studied here is important considering the range of estimates for c_0 reported for this system. At 45.5 and 45.0 at.% Ni the ac susceptibility data are unequivocal whereas the resistivity data are not (the latter shows a monotonically decreasing $\mathrm{d}\rho/\mathrm{d}T$ above 4.2 K and 2 K respectively in the 45.5 and 45.0 at.% Ni samples, although the resistivity in the 46 at.% Ni sample shows the effects of ordering above 4.2 K clearly, in agreement with previous reports [2]); figure 17 confirms that the LFRA measurements indicate the presence of ferromagnetic ordering in both of these samples (albeit at higher temperatures than the susceptibility data). These latter thus support our earlier assignment [22] of a critical composition *below* 45 at.% Ni; specifically $c_0 = 44.5$ at.% Ni for these samples.

Figure 18 shows a plot of T_C obtained from the analysis of the $\chi(H, T)$ data (presented in section 3.1.2) against the Ni concentration c; this allows a direct comparison with a similar plot with T_C values obtained from the zero-field susceptibility [27] (which did not admit exponent estimates). While the T_C values deduced from the latter are generally higher (partly attributable to the annealing of these samples at 550 °C—see section 3.3 below), the slope of the line drawn in figure 18 yields $\mathrm{d}T_C/\mathrm{d}c \simeq 8$ K (at.% Ni)$^{-1}$, in excellent agreement with that deduced from the zero-field data over the same composition range.

3.3. Effects of aging

As mentioned in the introduction, the properties of the CuNi system have been shown to vary with heat treatment and sample quench rate. The overall consensus that appears to have emerged from studies of the influence of annealing temperature, time, quench rate, cold-working and irradiation treatment is that samples quenched from temperatures above about 700 °C have a random Ni distribution, while subsequent lower-temperature annealing produces clustering (and a *higher* T_C [27]).

As part of the present study, an attempt has been made to investigate the effect of aging on cluster size and short-range order, with particular emphasis on the LFRA since this property seemed to display the influence of this latter order above T_C in a marked manner. Initially, the ac susceptibility was used to probe aging effects, specifically their influence on

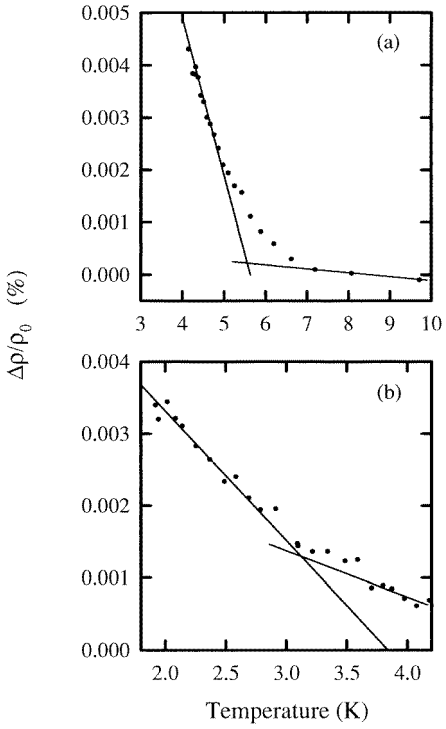

Figure 17. As in figure 15, for (a) the 45.5, and (b) 45 at.% Ni samples.

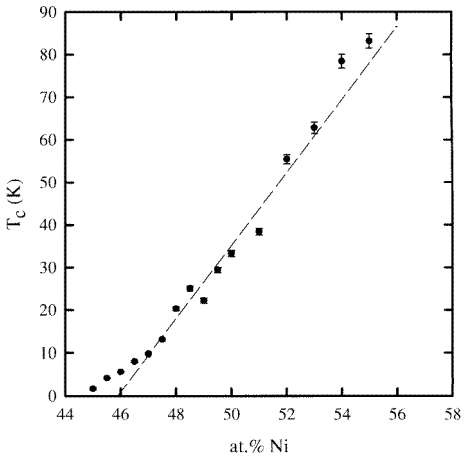

Figure 18. The T_C estimates from ac susceptibility (table 1) plotted against Ni concentration (in at.%).

T_C, by measuring $\chi(H_a, T)$ with $\mu_0 H_a = 0$ and 4 mT. The latter revealed (in samples with 45, 46, 47, 48, 50 and 55 at.% Ni) *no* change from the *as-quenched* state (from 950 °C) following aging for one week at room temperature. Consequently, the effects of subsequent low-temperature annealing at 200 °C were investigated; after being aged at this temperature

for predetermined intervals the samples were removed from the furnace and allowed to cool naturally. The slower cooling accompanying the latter produced irreversible changes. Initial measurements on a 48 at.% Ni sample were performed; these showed that successive anneals at 1 plus 1 plus 2 plus 4 hours (with a slow cool after each anneal) produced essentially the same change in the evolution of the 4 mT critical peak (in $\chi(H, T)$) as did a single 2 hour anneal and slow cool (of a virgin, as-quenched sample).

Consequently, this latter procedure was applied subsequently to all six samples studied (covering the entire compositional range fabricated); these changes are summarized in table 3 which indicates increases of less than 10% in $T_M(H)$ (the 4 mT critical peak temperature) in all samples studied (roughly equivalent to the changes in amorphous $Fe_{90}Zr_{10}$ following partial hydrogenation [44]).

Table 3. Effects of aging on the field-dependent susceptibility critical peak temperature measured in $\mu_0 H_a = 4$ mT before (T_p (K)) aging and after (T_p' (K)) and on the transport data; samples annealed for 2 h at 200 °C.

at.% Ni	T_p (K)	Anneal time at 200 °C (h)	T_p' (K)
45.0	1.83	2	2.00
46.0	6.85	2	7.10
47.0	10.6	2	11.6
48.0	22.4	2	23.6
50.0	35.3	2	36.6
55.0	83.5	2 + 4	86.6

	As quenched			Aged		
at.% Ni	T_C (K): LFRA	$A(\eta)$ (10^{-3})	T_C (K): $\rho(T)$	T_C (K): LFRA	$A(\eta)$ (10^{-3})	T_C (K): $\rho(T)$
46	8.2	0.30	7.2	8.6	0.33	—
47	10.5	0.44	10.3	11.3	0.43	10.8
48	20.2	0.96	19.6	21.4	0.96	19.7
50	33.4	1.6	31.5	35.2	1.6	32.1
55	86.0	4.6	83.1	87.5	4.6	86.4

The resistivity samples were subject to this same aging/annealing treatment, the results of which are also presented in table 3. Using the T_C values (obtained from the LFRA) contained in this latter part of the table, the LFRA data obtained before and after aging are compared in figure 19 for the 46 at.% Ni sample. This figure shows that the effects of the aging process induced here following quenching are minimal; T_C increases by less than 5% (table 3), A by 10% with a comparable enhancement in the 'tail' above T_C. Thus, while changes induced by aging/annealing at higher temperatures (400–650 °C) following quenching are significant [27], the present study shows that those produced by lower-temperature (200 °C) aging are not, even close to the critical composition.

4. Summary and conclusions

The results of detailed measurements of the field- and temperature-dependent ac susceptibility and the LFRA (both presented for the first time), supplemented by zero-field resistivity data, on (random) CuNi samples, indicate the presence of ferromagnetism at

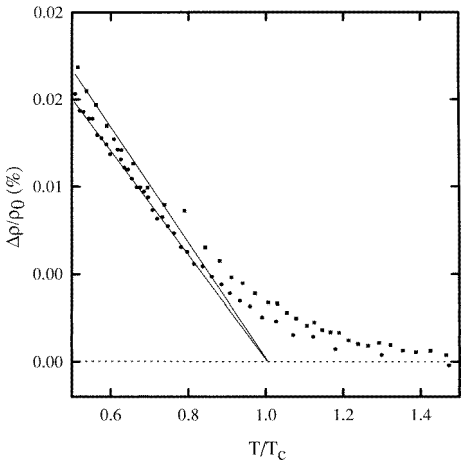

Figure 19. The LFRA plotted against reduced temperature for the 46 at.% Ni sample before (solid circles) and after (squares) aging. The corresponding estimates for T_C and slope A are summarized in table 3.

45 at.% Ni. The latter is consistent with a previous estimate of $c_0 = 44.5$ at.% Ni deduced from SRA measurements on the same samples. Many of the features presented above are consistent with a quasi-localized moment description of the system with a distribution of exchange coupling strengths between such moments. If this distribution is assumed to be Gaussian, the trends evident in exponent values deduced from $\chi(H, T)$ are consistent overall with the ratio η of the first (J_0) to second (J) moment of this distribution decreasing as the critical concentration is approached from above. Nevertheless, these data indicate that $\eta > 1$ at 45 at.% Ni, so that if a spin-glass-like phase is to appear at all in this system ($\eta < 1$), its range in composition and temperature is very limited ($c \leqslant 44.5$ at.% Ni, $T_{sg} \propto J < 2$ K). Indeed comparisons with the PdNi system suggest that such a phase may also be absent here.

The LFRA data are also consistent with such a model, which predicts that $A(\eta)$ should also fall as η decreases towards 1 (i.e. $c \rightarrow c_0$) and the limit of stability of the ferromagnetic phase is approached. However, the large variation reported for A (table 2) cannot be reproduced by model calculations [44] *unless* the ratio (D/V) in (10) increases by over an order of magnitude between c_0 and 55 at.% Ni; while the residual resistivity ρ_0 (and hence, by inference, V, changes in band structure notwithstanding) is known to fall over this range [21], this would have to be accompanied by large increases in D.

While the effects of aging/annealing are known to be complex in this system, the specific procedures utilized here lead, within the localized model described above, to an increase in J_0 ($T_C \propto J_0$) and η ($A(\eta)$ increases as η increases, again provided that other parameters are not significantly influenced), indicating that this aging process induces the first moment of this distribution to increase more rapidly than its width.

Acknowledgments

We are pleased to thank the Natural Sciences and Engineering Research Council (NSERC) of Canada for support in the form of operating and equipment grants (to GW) and fellowships (to PAS), and the International Nickel Company (INCO) for providing the pure Ni.

References

[1] Mott M F 1935 *Proc. R. Soc.* **47** 571
Kittel C 1971 *Introduction to Solid State Physics* (New York: Wiley)
[2] Houghton R W, Sarachik M P and Kouvel J S 1970 *Phys. Rev. Lett.* **25** 238
[3] Hicks T J, Rainford B D, Kouvel J S, Low G G and Comly J B 1969 *Phys. Rev. Lett.* **22** 531
[4] Kouvel J S and Comly J B 1970 *Phys. Rev. Lett.* **24** 598
[5] Robbins C G, Claus H and Beck P A 1969 *Phys. Rev. Lett.* **22** 1307
[6] Perrier J P, Tissier B and Tournier R 1970 *Phys. Rev. Lett.* **24** 313
[7] *Landolt–Börnstein New Series* 1982 Group III, vol 15 (Berlin: Springer) p 289 *et seq*.
[8] Lederer P and Mills D L 1968 *Phys. Rev.* **165** 837
[9] Kaiser A B and Doniach S 1970 *Int. J. Magn.* **1** 11
[10] Blandin A 1973 *Magnetism* vol 5, ed G T Rado and H Suhl (New York: Academic)
[11] Hirst L L 1970 *Phys. Kondens. Materie* **11** 255
Williams G 1976 *Solid State Commun.* **19** 821
[12] Loram J W and Mirza K A 1985 *J. Phys. F: Met. Phys.* **15** 2213
[13] Murani A P, Tari A and Coles B R 1974 *J. Phys. F: Met. Phys.* **4** 1769
[14] Tari A and Coles B R 1971 *J. Phys. F: Met. Phys.* **1** L69
[15] Kunkel H P, Wang Z and Williams G 1987 *J. Phys. F: Met. Phys.* **17** L157
Kunkel H P, Wang Z and Williams G 1989 *J. Phys.: Condens. Matter* **1** 3381
[16] Aldred A T, Rainford B D and Stringfellow M W 1970 *Phys. Rev. Lett.* **24** 897
[17] Chouteau G, Tournier R and Mollard P 1974 *J. Physique* **35** C4 185
[18] Chouteau G 1976 *Physica* B **84** 25
[19] Sain D and Kouvel J S 1978 *Phys. Rev.* B **17** 2257
[20] Cheung T D, Kouvel J S and Garland J W 1981 *Phys. Rev.* B **23** 1245
[21] Ododo J C and Coles B R 1977 *J. Phys. F: Met. Phys.* **7** 2393
[22] Stampe P A and Williams G 1997 *J. Phys.: Condens. Matter* **9** 9251
[23] Claus H 1975 *Phys. Lett.* **51** A 283
[24] Hicks T J 1977 *J. Phys. F: Met. Phys.* **7** 481
[25] Maartense I and Williams G 1978 *Phys. Rev.* B **17** 377
Sarkissian B V B 1981 *J. Phys. F: Met. Phys.* **11** 2191
[26] Williams G 1991 *Magnetic Susceptibility of Superconductors and Other Spin Systems* ed R A Hein *et al* (New York: Plenum) p 475
[27] Tranchita C J and Claus H 1978 *Solid State Commun.* **27** 583
Carnegie D W, Tranchita C J and Claus H 1979 *J. Appl. Phys.* **50** 7318
[28] Maartense I 1970 *Rev. Sci. Instrum.* **41** 657
[29] Osborn J A 1945 *Phys. Rev.* **67** 351
[30] Campbell I A, Fert A and Jaoul O 1970 *J. Phys. C: Solid State Phys.* **3** S95
Friederich A and Fert A 1974 *Phys. Rev. Lett.* **33** 1214
Hamzic A, Senoussi S, Campbell I A and Fert A 1978 *J. Phys. F: Met. Phys.* **8** 1947
Campbell I A and Fert A 1982 *Ferromagnetic Materials* vol 3, ed E P Wohlfarth (Amsterdam: North Holland)
[31] Kunkel H P, Roshko R M, Ruan W and Williams G 1991 *Phil. Mag.* B **63** 1213
[32] Berndt A G, Chen X, Kunkel H P and Williams G 1995 *Phys. Rev.* B **52** 10 160
[33] Chikazumi S 1997 *Physics of Ferromagnetism* 2nd edn (Clarendon: Oxford) p 486
[34] Ho S C, Maartense I and Williams G 1981 *J. Phys. F: Met. Phys.* **11** 699
[35] Wang Z, Kunkel H P and Williams G 1990 *J. Phys.: Condens. Matter* **2** 4173
[36] Kunkel H P, Roshko R M and Williams G 1988 *Phys. Rev.* B **37** 5880
[37] Stanley H E 1971 *Introduction to Phase Transitions and Critical Phenomena* (Clarendon: Oxford)
[38] Wang Z, Kunkel H P and Williams G 1992 *J. Phys.: Condens. Matter* **4** 10 385
[39] Roshko R M and Williams G 1984 *J. Phys. F: Met. Phys.* **14** 703
[40] LeGuillou L C and Zinn-Justin J 1980 *Phys. Rev.* B **21** 3976
[41] Kaul S N 1985 *J. Magn. Magn. Mater.* **53** 5
[42] Kornik K, Kunkel H P, Roshko R M and Williams G 1990 *Solid State Commun.* **76** 993
[43] Saran M and Williams G 1987 *J. Phys. F: Met. Phys.* **17** 731
[44] Stampe P A, Kunkel H P and Williams G 1993 *J. Phys.: Condens. Matter* **5** L625
Stampe P A, Kunkel H P and Williams G 1994 *J. Phys.: Condens. Matter* **6** 3045
[45] Kawatra M P and Budnick J I 1970 *Int. J. Magn.* **1** 61